CHAPTER 6

Effect of MnO_2 Additive on the Crystal Structure, Microstructure, Ferroelectric, Piezoelectric and Dielectric Properties of (1-x)$Ba(Cu_{1/3}Nb_{2/3})O_3$-(x)$PbTiO_3$ Ceramics

CHAPTER 6.

Effect of MnO_2 Additive on the Crystal Structure, Microstructure, Ferroelectric, Piezoelectric and Dielectric Properties of $(0.38)Ba(Cu_{1/3}Nb_{2/3})O_3$-$(0.62)PbTiO_3$ Ceramics

6.1 Introduction

The high responses in the dielectric and piezoelectric properties near MPB compositions of the piezoelectric ceramics comes from the softening of the crystal lattice in the phase coexistence region where usually a monoclinic or other low symmetry phases are found. These low symmetry phases provide an increased number of favourable directions for polarization reversal and the flattening of the free energy due to local structural modifications [5,85,99,116]. Apart from the design and inclusion of MPB into solid solutions, other approaches like defect engineering, chemical substitutions/additives, textured grain orientations, etc., are among some other promising ways to further enhance the ferroelectric and piezoelectric responses of materials. In defect engineering, the defects are created and controlled by introducing ions of different valences and sizes in both stoichiometric and non-stoichiometric ways and/or creating cationic and anionic vacancies through heat treatment processing such as prolonged annealing and quenching [45]. Many dopants, such as oxides of Mn, Fe, Mg, La, Ce, Sb, etc., are famous for inducing variation in the characteristics of perovskite materials. Especially the leakage current, which is undesirable for the good piezoelectric and ferroelectric properties, can be tuned by the non-stoichiometric incorporation of these ions.

The doping effect of MnO_2 has been vastly studied in literature on many binary and ternary perovskite solid solutions, in which its effect has been looked at sintering temperature (densification), grain growth, dielectric, piezoelectric, ferroelectric and electrocaloric properties [47,50,142–148]. On one hand, improvements in densification, dielectric losses (tanδ), mechanical quality factor (Q_m) and grain growth have been observed in most of the studies, while on the other hand, the ferroelectric and piezoelectric properties may improve or deteriorate, depending on the type of additives and their concentration [12-20]. Manganese ions with variable valences have been incorporated in perovskite structures in a variety of ways, such as by partial substitution of a cation or as an additive in the form of oxides (MnO/MnO_2) or carbonates ($MnCO_3$) [144,145,149,150].

Studies on Mn doping in perovskite-type materials have shown that the increasing concentration of Mn promotes cubic nature and reduces the ferroelectric distortion of the crystal lattice [152,153], which in consequence, can induce a decrease in Curie temperature [154]. This fact can be used to induce a greater number of possible phase boundary regions, tri-critical and quad-critical points in the phase diagrams containing rhombohedral, monoclinic and tetragonal phases around MPBs. In this way, Mn doping can also create an additional softening effect. Recent studies have shown that the triple and quadruple points in the phase diagram surrounded by multiple phases in a small region having a low free energy barrier between such phases can be a key to inducing high responses of dielectric and piezoelectric properties in ceramic perovskite solid solutions [42,75].

In this chapter, the effect of MnO_2 additive on a selected composition of (1-x)BCN-(x)PT ceramics has been studied to know its impact on crystal structure,

microstructure and various physical properties. As discussed in chapter 3, there are multiple MPBs in (1-x)BCN-(x)PT ceramics, spread across a wide range of compositions. The (0.38)BCN-(0.62)PT composition has been chosen, as it lies close to an MPB. Non-stoichiometrically added dopants or additives are assumed to be partially dissolved in the lattice of the parent compound at low concentrations due to diffusion at higher temperatures. However, at higher concentrations, the additives may lead to the formation of secondary phases. Additionally, an effort has been made to comprehend the low-concentration properties and phenomena using analogical predictions of higher-concentration ones.

6.2 Crystal Structure Modifications in (0.38)BCN-(0.62)PT Ceramics by MnO_2 additive

The (0.38)BCN-(0.62)PT compositions with excess MnO_2 additive in 0.5, 1, 4 and 8 wt% of the total stoichiometric weight, were prepared by solid state ceramic method as discussed in chapter 2. The resulting compositions are abbreviated as “Pure”, Mn05, Mn1, Mn4 and Mn8, respectively, in this chapter. Fig 6.1(a) shows the XRD patterns of “Pure”, Mn05, Mn1, Mn4 and Mn8 compositions. The magnified view of the diffraction pattern showing the development of the (200) pseudocubic XRD profile for each composition is also shown in the inset of Fig 6.1(a). A considerably high 4wt% addition of MnO_2 (Mn4) manages to accommodate itself in the material without any noticeable secondary phase peak in the XRD pattern. However, the 8wt% excess MnO_2 leads to the appearance of a small secondary phase of $Cu_{1.5}Mn_{1.5}O_4$ along with the perovskite phase. The phase fraction of this impurity is about 1%, and a small corresponding XRD peak is marked by an asterisk in Fig 6.1(a). It is clear from the

figure that even a small amount of MnO_2 addition can significantly affect the crystal structure of the material [see inset of Fig 6.1(a)].

The crystal structure of the pure phase (0.38)BCN-(0.62)PT composition is expected to be tetragonal by visual inspection of the splitting of the XRD peaks. However, there is a significant broadening of many diffraction peaks and diffuse scattering between split XRD profiles. Two coexisting tetragonal phases explain the crystal structure of "Pure" composition, as discussed in Section 3.5.3 of chapter 3. The coexistence of two tetragonal crystal structures indicates a typical crystallographic phase separation in the solid solution. The characteristics of the end components dominance appear due to which two slightly different phases appear whose crystal structures are modified by the accommodation of the lattice distortion.

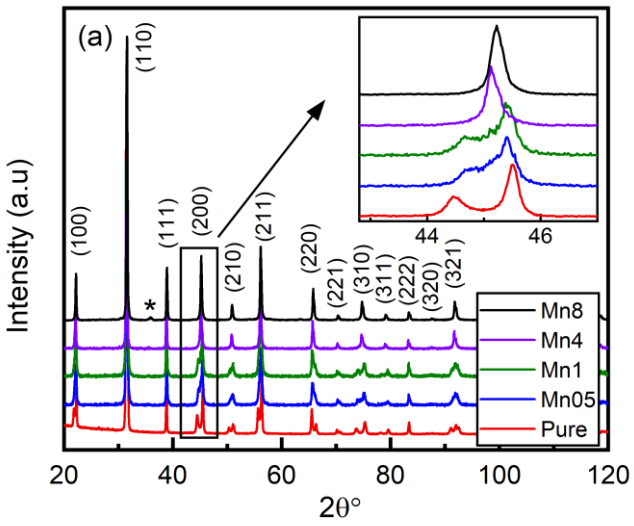

Fig 6.1 Powder XRD patterns of (0.38)BCN-(0.62)PT (Pure) ceramics with different MnO_2 additive concentrations. The inset shows the zoomed portion for the (200) pseudocubic XRD profile

Similar to the pure composition of (0.38)BCN-(0.62)PT, the crystal structures of MnO_2 added compositions, Mn05, Mn1, Mn4 and Mn8, have also been analyzed by Rietveld structure refinement considering a two-phase coexistence model. The XRD

patterns of Mn05 and Mn1 compositions fit well by considering two co-existing tetragonal phases. It is evident from the inset to Fig 6.1(a) that, increasing the MnO_2 addition decreases the angular splitting of the XRD peaks for tetragonal structure, and for Mn8 composition, all the XRD peaks appear as singlets. The Rietveld structure refinement for the Mn4 composition reveals a coexistence of tetragonal (Phase 2) and cubic phases (Phase 1) in the *P*4*mm* and *Pm*-3*m* space groups, respectively. The crystal structure of the (0.38)BCN-(0.62)PT solid solution behaves like two different crystallographic phases coexisting together, even after the incorporation of the MnO_2 additive. The crystal structure of Mn8 can be fitted well by considering a single cubic structure in the *Pm*-3*m* space group. The Rietveld fits for Mn05, Mn1, Mn4 and Mn8 compositions in the 2θ range 20°-120º are shown in Fig 6.2(a-d). A very decent fit between the observed and calculated XRD patterns, further confirms the correctness of the considered crystal structures. The lattice parameters, unit cell volume, phase fraction and Rietveld agreement factors of Mn-added compositions are listed in Table 6.1 for MnO_2-added compositions. The low values of the chi-square parameter, also reflect the excellent Rietveld fit for all compositions.

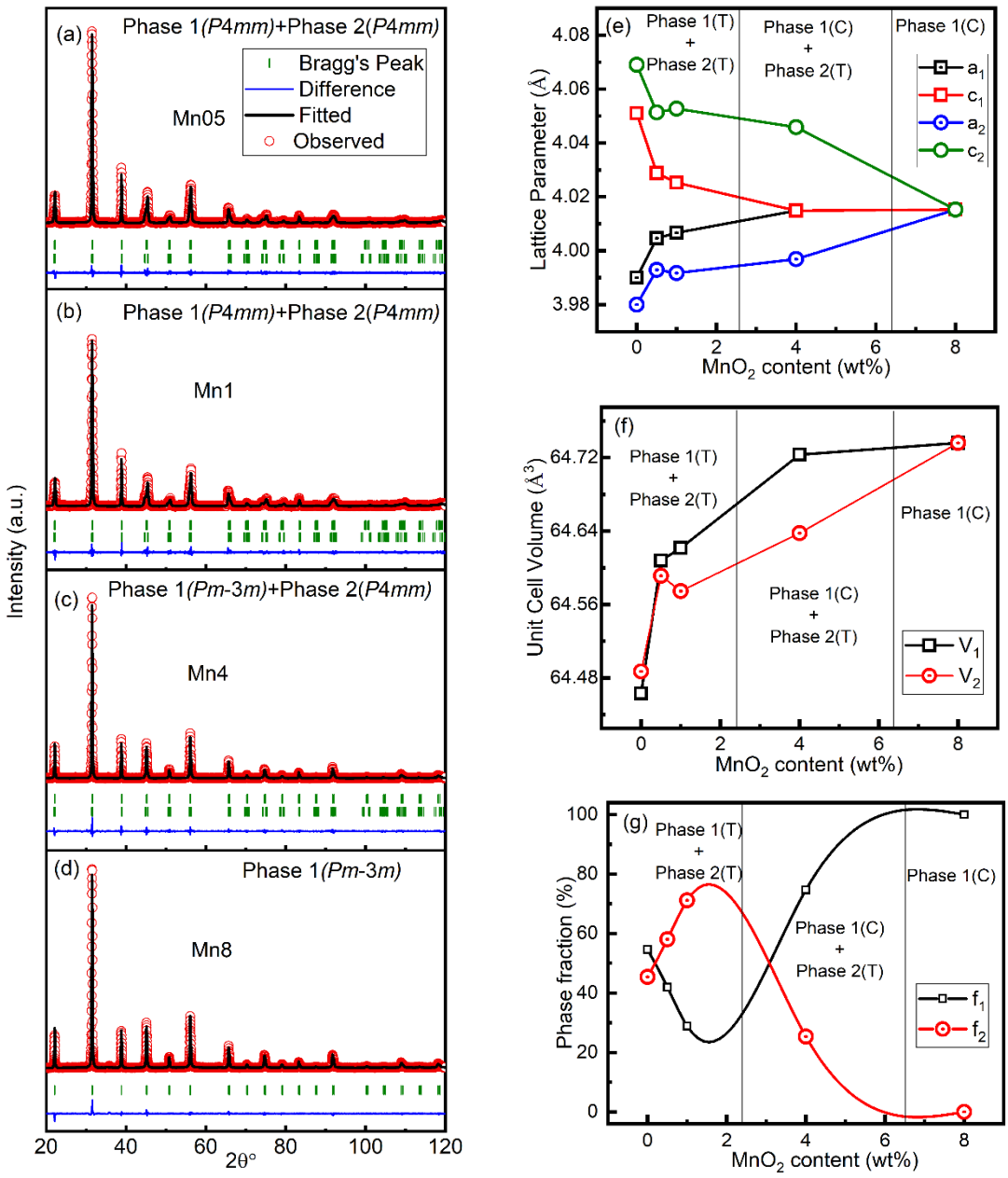

Fig 6.2 Rietveld fitted XRD patterns of (a) Mn05, (b) Mn1, (c) Mn4 and (d) Mn8 compositions; (e) lattice parameter, (f) unit cell volume and (g) phase fraction variation of "pure" and MnO_2 added (0.38)BCN-(0.62)PT ceramics

Table 6.1 Crystal structural parameters obtained from Rietveld structure refinement for Mn05, Mn1, Mn4 and Mn8 compositions.

Composition		Mn05		Mn1		Mn4		Mn8
Crystal System		Phase1[T]	Phase2[T]	Phase1[T]	Phase2[T]	Phase1[T]	Phase2[C]	Phase2[C]
Lattice Parameter	a(Å)	4.0063(3)	3.9925(1)	4.003(3)	3.9915(1)	4.0149(1)	3.9975(4)	4.0152(6)
	c(Å)	4.0271(5)	4.0513(3)	4.027(6)	4.0533(3)		4.0448(5)	
Unit Cell Volume($Å^3$)		64.640(1)	64.582(6)	65.77(6)	64.560(1)	64.721(3)	64.638(4)	64.734(2)
Phase fraction (%)		41.7(9)	58.2(8)	74.2(9)	25.7(9)	75.51(4)	25.41(6)	100
R_{wp}		14.4		15.0		14.8		9.41
R_p		10.3		11.2		10.9		6.91
χ^2		1.28		1.25		1.22		1.91

Fig 6.2(e-g) shows the variation of lattice parameters, unit cell volume and phase fraction obtained from Rietveld crystal structure refinement as a function of wt% of MnO_2 additive. In several papers in existing literature on Mn incorporation in the perovskite lattice, a trend has been observed that the crystal structure symmetry of the solid solution tends to become more symmetric as one increases the concentration of the Mn [152,153]. A similar observation has been found in our results also, as evidenced from Fig 6.2(e). The tetragonal distortion of both the co-existing phases decreases continuously, except for a slight increase in Mn1 for one of the co-existing phases. The unit cell volume is shown for both the phases in Fig 6.2(f) illustrates that it has mostly increasing trend with an increase in MnO_2 additive, indicating the expansion of the unit cell. Only a tiny decrease in unit cell volume is observed in Mn1. The differences in unit cell volume of the two phases are more significant in Mn1 and Mn4. Fig 6.2(g) illustrates that the phase fraction of low tetragonality lattice initially decreases up to Mn1 and then increases with increasing additive concentration.

6.3 Microstructural Studies

Fig 6.3(a, b, c, d and e) depicts the SEM micrographs of the sintered (1050^{o}C for 2 hours) surface of “Pure”, Mn05, Mn1, Mn4 and Mn8 pellets, respectively, while internal cross-section images on fractured surface of “Pure” and Mn8 pellets are shown in Fig 6.3(f and g). The average grain size of the “Pure” composition is around 0.9µm [see Fig 6.3(h)], which increased to approximately 2µm and 2.7µm in the Mn05 and Mn1 compositions, respectively. The local surface melting of the grains in liquid phase sintering of the Mn05 and Mn1 causes the differential contrast of the respective images and irregular shapes [126]. In Mn4 composition, the average grain size is reduced to 1.5µm, probably due to the changed growth rate for the co-existing tetragonal and cubic phases. The pellet surface of Mn8 had circular and elongated grains, as can be seen in Fig 6.3(e). However, its internal cross-section image depicted in Fig 6.3(g) on a fractured surface, shows a bimodal grain size distribution and the elongated grain lies mostly at the surface. The histogram in Fig 6.3(h) shows the grain size distribution of internal structure of both “Pure” and Mn8. On one hand, Mn doping helps increase sintering ability and grain growth, whereas, on the other hand, the presence of Nb-ion, as a grain size inhibitor, can pose restrictions on the increment of grain size [145,155]. The influence of these competing factors might be the reason for the first increase and then decreases of the grain size.

Along with the grain size variation, a shape variation in the grains can also be witnessed in various compositions. The grain shape of Mn05 and Mn1 compositions has irregular polygons due to partial surface melting, whereas a spherical-type grain structure can be seen in Mn4. Additionally, some sharp-edged cube-type and rectangular rod-like elongated grain structures are also visible in Mn4 and Mn8. The

non-stoichiometric addition of additives has a solubility limit that can be incorporated within the lattice of a compound/solid solution, after which they start forming secondary phases that may typically get deposited at the grain boundaries [148,156]. In the microstructure of the Mn8 sample, an abundance of elongated grains is seen along with the regular rounded grains. An impurity phase is also present in Mn8 (as revealed by XRD studies), which might be responsible for the bimodal evolution of the grains in the Mn8 composition, as shown in Fig 6.3(e).

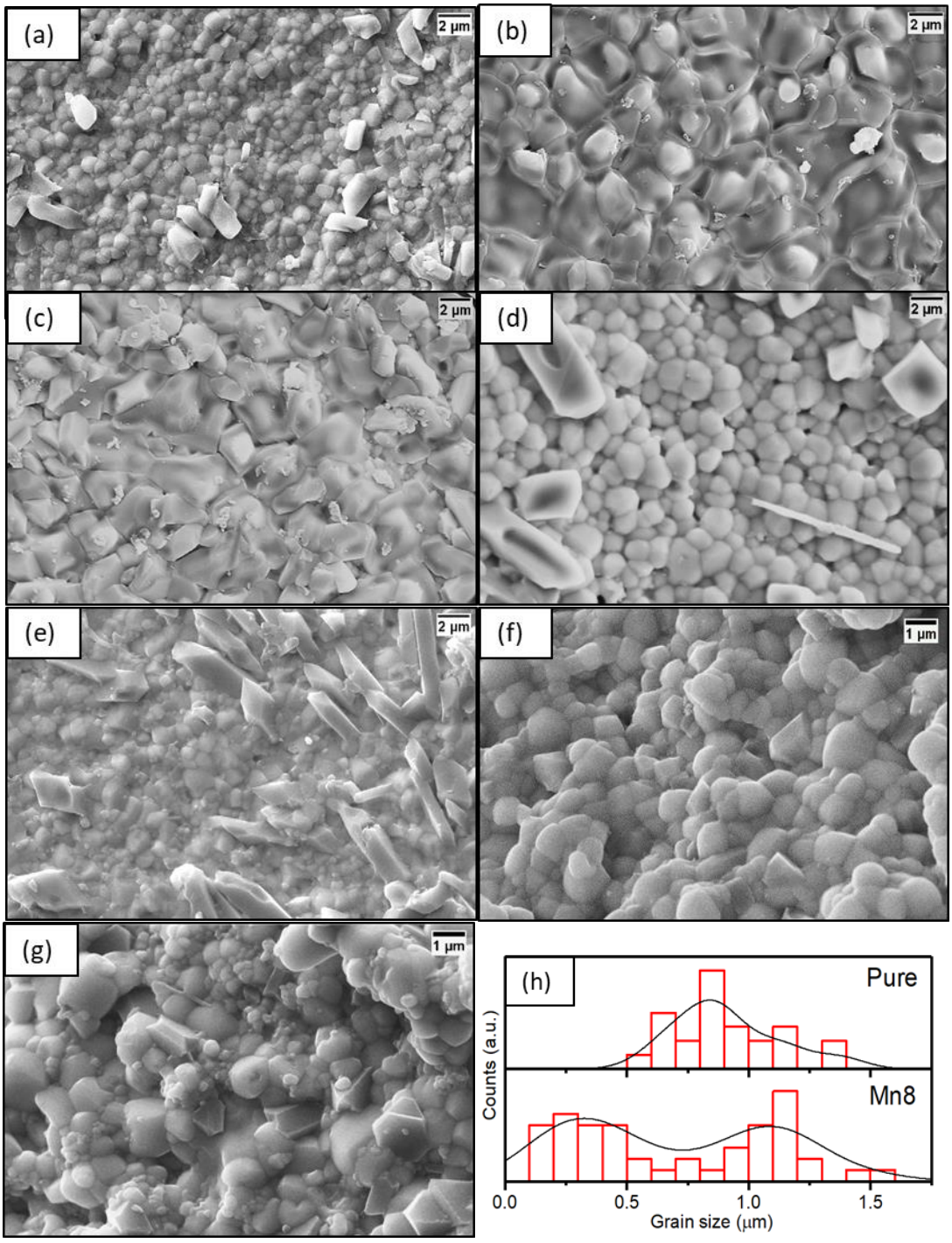

Fig 6.3 SEM micrograph of pure and MnO_2 added (0.38)BCN-(0.62)PT pellets, sintered at 1050°C for 2 hours; Pellet surface image at 10KX magnification for (a) "Pure", (b) Mn05, (c) Mn1, (d) Mn4 and (e) Mn8 ceramics; Internal cross-section of fractured pellet surface for (f) "Pure" and (g) Mn8 ceramics at 20KX magnification; (h) Histogram of grain size distribution calculated from internal cross-section images of "Pure" and "Mn8" ceramics

6.4 EDS Studies

The EDS spectra of Mn8 composition have been recorded in different microstructure regions (elongated rectangular rod-like grains and the area containing rounded grains) to find out the compositional variations existing among them. Fig 6.4(a) and (b) depict the histograms for the atomic weight % of the various elements as per the nominal composition (black) and that determined experimentally from EDS (grey), for rounded grain area and elongated grain structures, respectively. EDS analysis reveals that there are indeed slight compositional differences between the two types of grain structures. The rounded grain microstructure is in good agreement with the nominal concentrations of the respective elements for Mn8 composition. However, the histogram corresponding to the elongated grain sites (Fig 6.4(b)) suggests the formation of a Cu-rich phase. This conclusion is also consistent with the XRD data of Mn8, where a Cu-rich impurity phase, $Cu_{1.5}Mn_{1.5}O_4$, has been found. Slight Nb-ion imbalance has also been observed from the EDS. Although the accuracy of the atomic concentration of ions from EDS is not very high, a relative comparison can still be made.

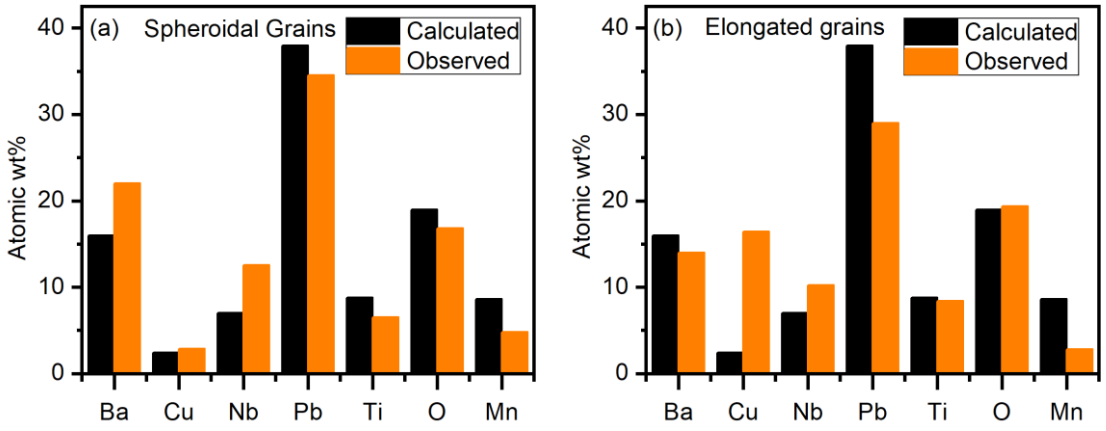

Fig 6.4 Histogram depicting the atomic weight % of the various elements as per the nominal composition (black) and that determined experimentally from EDS (orange) at (a) rounded and (b) elongated grain regions of the sintered pellet of Mn8

6.5 Results of XPS Studies

X-ray photoelectron spectroscopic (XPS) studies have been carried out to examine the chemical state of the elements in the pure and with MnO_2 additive composition of the solid solution. Fig 6.5(a, b and c) displays the XPS spectra of B-site cations of the "Pure" (or 0.62 composition) [Fig 6.5(a_1, b_1 and c_1)] and Mn1 [Fig 6.5(a_2, b_2 and c_2)] samples, for Cu-2p, Nb-3d and Ti-2p orbitals. The 2p spectra of Cu^{+2} states also have strong shake-up satellites around 942.4eV, 944.6eV and 963.3eV [129]. However, only weak satellites are observed in the XPS spectra of the Cu^{+1} ion as shown in Fig 6.5(a). The peaks in the XPS spectra of Cu-$2p_{3/2}$ also differ in the FWHM, i.e., Cu^{+2} peaks are slightly broader than Cu^{+1} peaks [129]. Additionally, in Auger Cu LMM spectra, the standard CuO and Cu_2O exhibit a characteristic peak at Kinetic Energy of 917.1eV and 916.3eV, respectively [129]. The peaks of Cu LMM spectra in Cu^{+1} and Cu^{+2} possess a small difference of approximately 0.8eV between them. In the samples, the peaks corresponding to Cu-$2p_{3/2}$ and Cu-$2p_{1/2}$ have been observed at around 933.7eV and 953.6eV, respectively, for both the "Pure" and Mn1 compositions [see Fig 6.5(a_1 and b_1)]. A small deviation from the standard value of B.E. is attributed to the differing crystal field. The respective Cu LMM Auger spectra are also shown in the inset of these plots. Both the compositions have these peaks at around 918eV, which indicates that the majority of copper is in the +2 state. Because of the overlapping peaks, the existence of a small amount of Cu^{+1} ionic state along with Cu^{+2} cannot be confirmed by visualizing either the Cu-2p spectra or the Auger Cu LMM spectra.

The spin-orbit coupling splits the XPS spectra for the Nd-3d peak into $3d_{5/2}$ and $3d_{3/2}$. For Nb^{+4} and Nb^{+5}, the B.E. of $3d_{5/2}$ lies around 209.3eV and 206.6eV in the perovskite structure [130]. The values slightly differ from a Nb_2O_5 compound, which

has B.E. 207eV for $3d_{5/2}$. In Fig 6.5(b_1) and (b_2), the XPS spectra corresponding to the Nb-ion for the "Pure" and Mn1 compositions are shown. The "Pure" sample has only the '+5' valence state of Nb, whereas the existence of both '+5' and '+4' valency is visible in Mn1 with the identical B.E. splitting of 2.7eV between $3d_{5/2}$ and $3d_{3/2}$ states. The approximate concentration of Nb-ion in '+5' and '+4' states is 94% and 6%, respectively.

The Ti-2p XPS spectra of TiO_2 have two components in B.E. peaks ($2p_{3/2}$ and $2p_{1/2}$). These are separated by approximately 5.7eV, 5.2eV and 5.6eV for Ti^{+4}, Ti^{+3} and Ti^{+2} valence states, respectively [131]. The B.E. of the different chemical states of Ti-ion is different, such as the B.E. of $2p_{3/2}$ for Ti^{+4} is 458.7eV (±1.3eV [132]), Ti^{+3} is 457.2eV and Ti^{+2} is 455.2eV [131,157]. The B.E. peaks have been observed at 458eV and 463.5eV [see Fig 6.5(c_1) and (c_2)] by fitting the XPS spectra of Ti-ion in the "Pure" compound. The separation is comparable to that observed in standard TiO_2, confirming the '+4' state in the "Pure" sample. Similarly, in Mn1 composition, the characteristic separation has been found between the $2p_{3/2}$ and $2p_{1/2}$ peaks as 5.7eV, 5.2eV and 5.6eV, indicating the presence of '+4', '+3' and '+2' states with an approximate ratio of 81%, 12% and 7%, respectively. However, it should be noted that the quantitative estimation of the presence of Ti^{+3} and Ti^{+2} states is highly dependent on the choice of background and, therefore, should be treated with caution.

Since the concentration of Mn-ions is low in Mn05 and Mn1, it is difficult to observe any intense Mn-ion peaks for them. Therefore, an approach of analysing high-concentration MnO_2 added samples for the analogical extension of the phenomena in the low-concentration MnO_2 added compositions have been used. Due to the presence of the impurity phase in Mn8, it has been ignored for XPS analysis and Mn4

composition has been used. The XPS of Mn-2p does not provide any helpful evidence regarding the differentiation of the presence of various Mn valences; however, the Mn-3s spectra can shed some light on it. Fig 6.5(d) shows the Mn-3s spectra of the Mn4 composition. Evaluating the exact percentage of the different valences of Mn-ion is difficult due to several reasons, such as the small concentration of Mn in the sample, the overlapping peaks of Ba-4d, Pb-5p and Cu-3p orbitals and the choice of the background for fitting the peaks. Still, a qualitative analysis the Mn4 sample can be done.

The Mn-3s peak splits due to the interaction between non-ionized 3s electrons and 3d valence band electrons. The energy difference between these peaks is around 6eV in Mn^{+2} states and 4.7eV for Mn^{+4} states, whereas the same is greater than 5.2eV in the case of Mn^{+3}. Typically, one sees a monotonic rise in splitting as valence states increase [158,159]. The difference between the two signature peaks of Mn-3s for Mn4 sample has been observed to be 4.7eV, 5.3eV and 6eV, which correspond to Mn^{+4}, Mn^{+3} and Mn^{+2}, respectively. Therefore, the Mn4 sample may contain all three oxidation states of Mn-ion. Additionally, the variable valences of Mn-ion have been widely observed in similar kinds of solid solutions upon adding MnO_2 as well as MnO [150]. Therefore, it is safe to assume the existence of Mn-ion in variable valences.

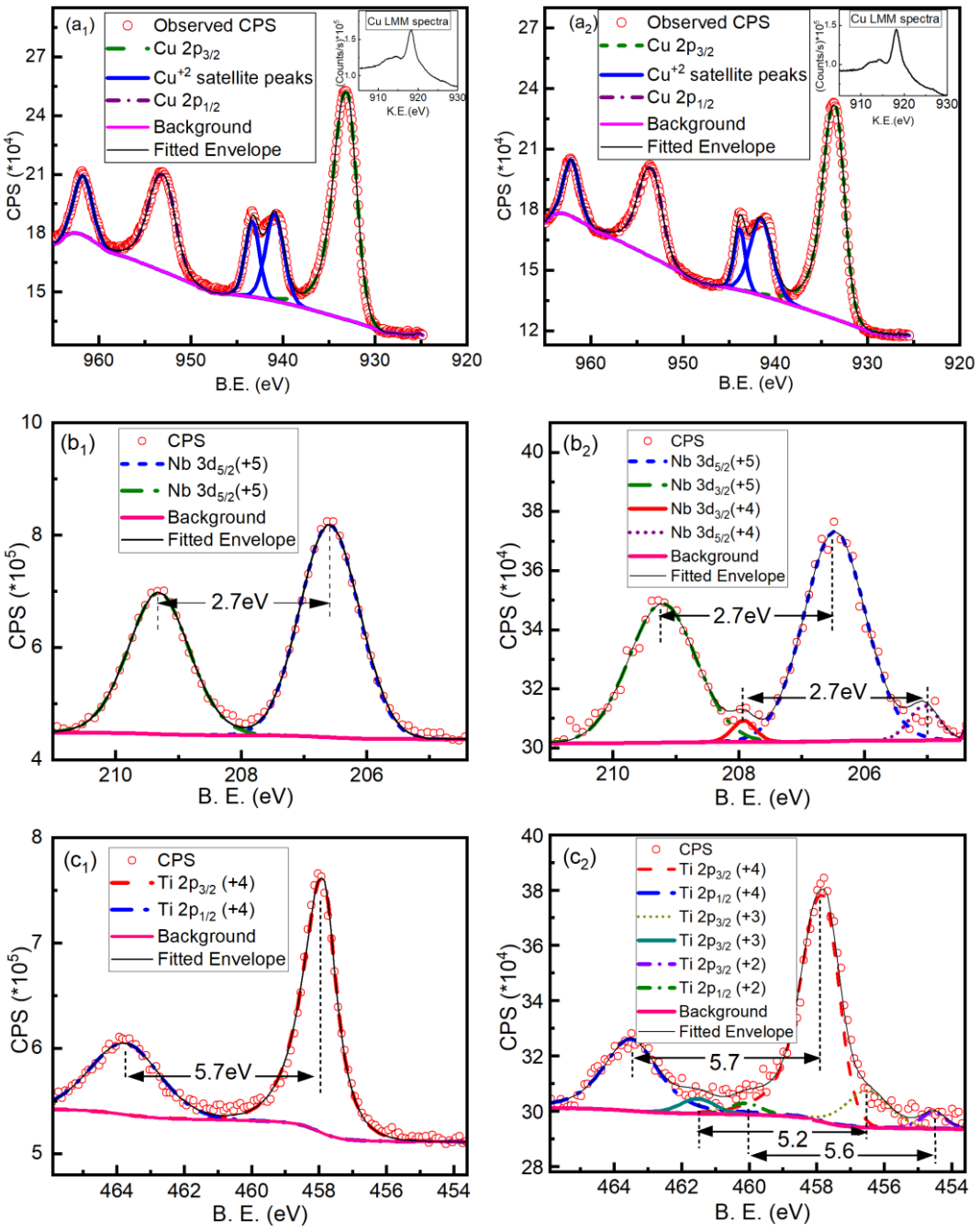

Fig 6.5 XPS spectra of (a) Cu-2p, (b) Nb-3d, (c) Ti-2p of “Pure” (left panel) and Mn1 (right panel)

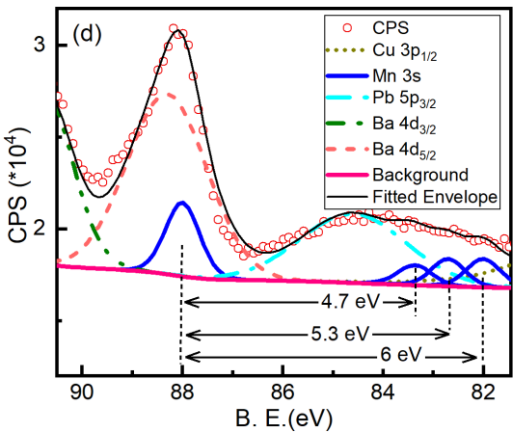

Fig 6.5 (d) XPS spectra of Mn-3s spectra of Mn4

The XPS spectra of O-1s have been collected for the investigation of the chemical state of oxygen. The XPS of the "Pure" sample examined both before and after annealing in the air atmosphere at 500°C is shown in Fig 6.6[(a) and (b)], respectively. The characteristic XPS peak of oxygen bound in the lattice for metal oxides has a B.E. between 529 and 530eV [128]. In our case, the lattice oxygen peak has been observed at around 529.5eV for all the samples. The annealing in an air atmosphere has not altered the surface chemistry of the samples effectively. The higher binding energy shoulder to the lattice oxygen peak is generally attributed to the surface adsorbed adventitious hydroxyls of water [128]. A high oxygen vacancy level enables a surface to have more positively charged ions. Such a surface is favourable for the attachment of water molecules, and the likelihood of adsorption can be expected to increase. Moreover, it is reported that BCN is also difficult to synthesize in pure phase form, as it is prone to producing oxygen-deficient compounds [59]. Adsorption of hydroxyls and the creation of oxygen vacancies both have comparable energies of about 1eV [128]. The Mn-ion doping in BCN has also been reported to balance the artefacts of copper and oxygen formed in the perovskite phase [160]. An approximate 1eV activation energy corresponding to the oxygen vacancy relaxation is also determined

from the dielectric relaxations of the samples. Even though a representative quantitative assessment of the oxygen vacancy for the bulk volume of the material is not achievable by XPS characterization, the above-stated remarks suggest that the synthesised materials may have significant oxygen vacancies. If the ordinarily adsorbed water is assumed to be almost equivalent in all the samples, then the reduction in the height of the O-1s peak shoulder for Mn1 and Mn4 in Fig 6.6[(c) and (d)] may be correlated to the decrement in the oxygen vacancies after addition of MnO_2.

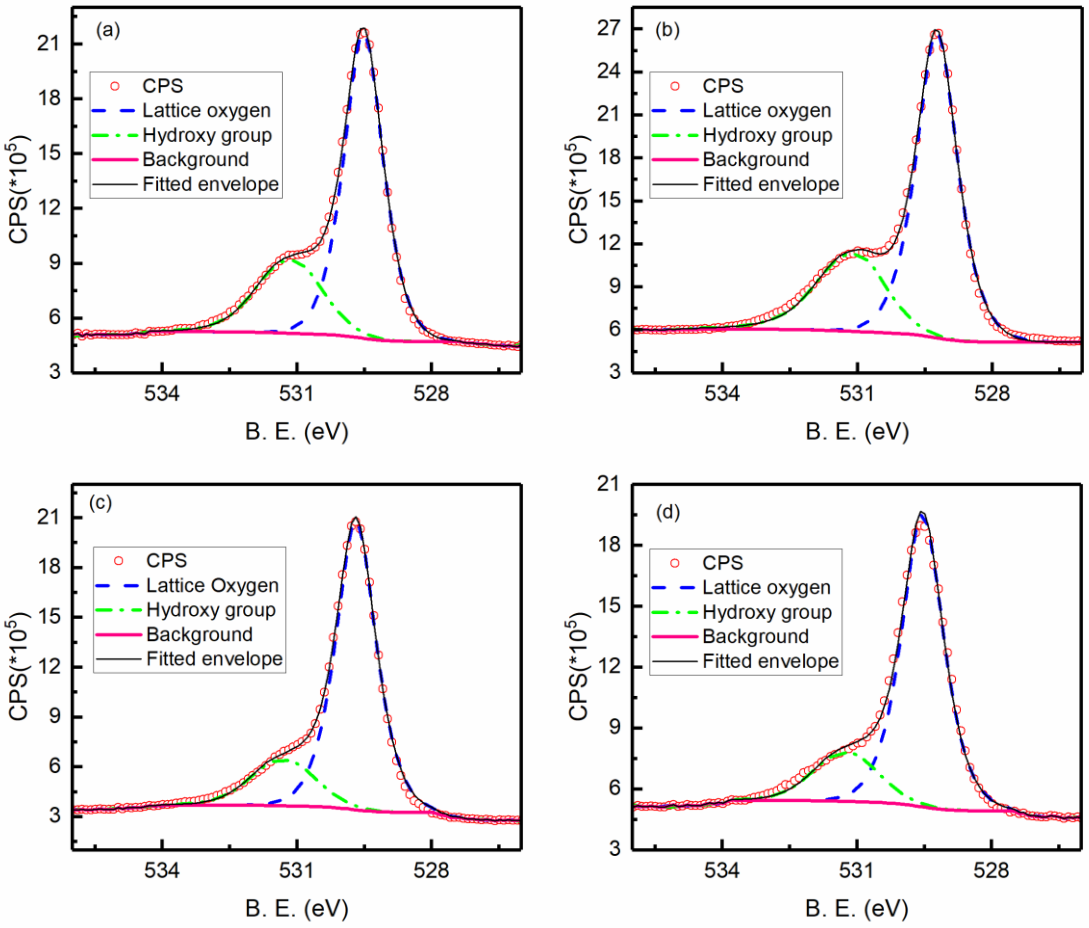

Fig 6.6 XPS spectra of O-1s of (a) "Pure" without annealing and (b) "Pure" after annealing; O-1s of (c) Mn1 and (d) Mn4

6.6 Defect Chemistry for the MnO_2 added (0.38)BCN-(0.62)PT Ceramics

The presence of the charged defect species strongly affects the electrical and electronic properties, and their identification can help the structure-property correlations of defect-engineered perovskite oxide ceramics. The accurate analysis of defect chemistry became quite complex in the present investigation, mainly for the following reasons: (i) The presence of more than one ion having multiple valence states, i.e. Cu(+1), Cu(+2); Mn(+2), Mn(+3), Mn(+4); Ti(+2), Ti(+3), Ti(+4) and Nb(+4), Nb(+5). (ii) The type of Mn incorporation as additive rather than substitutional. (iii) The processing of materials at high temperatures also induces the evaporation of Pb and O from the solid solution. The evaluation of the possibility of replacing a typical lattice ion with an additive ion and the percentage of ions replaced are both varying parameters that are difficult to ascertain. To explain the defect chemistry of these samples, the resulting phenomena in high shares of MnO_2 added compositions, i.e., Mn4 and Mn8, have been analysed. Due to large ionic radii, Pb and Ba undoubtedly occupy the A sites with similar ionic radii in 12 coordination (Pb^{+2} =1.49Å and Ba^{+2} =1.6Å). Considering the Shannon ionic radii (R) values in the octahedral site for different ions in different oxidation states are considered, it is clear that due to the comparable ionic radii of the Mn-ion to the B-site cations, Mn will occupy the B site alongside Cu, Nb or Ti sites, for any possible substitution due to diffusion at high temperatures [161].

The existence of ions with multiple valences in the solid solution matrix can potentially form charged defect species. Based on our observations of EDS, in which the concentration of Nb and Cu is more than the nominal composition value, it has been considered that the incorporation of Mn-ions is only being done at Nb and Cu sites. The

Cu^{+1}, Cu^{+2}, Nb^{+4} and Nb^{+5} ions have been considered as the hosts (based on the XPS analysis of Mn1), and they can be replaced by any of the Mn^{+2}, Mn^{+3} and Mn^{+4} ions (based on the XPS analysis of Mn4). The possible preference for B-site occupation can be predicted by the Hume-Rothery rule [153]. According to this rule, if the percentage ionic size difference (D_r) described in equation (6.1) is less than 15%, it is more likely to be present at the B site.

$$D_r(\%) = \frac{|R(dopant) - R(host)|}{R\,(host)} * 100 \qquad (6.1)$$

Types of charged defects produced by the replacement of different ions can be discussed using Kröger-Vink notation [162]. In Table 6.2, the D_r values as well as the defect type by writing a corresponding Kröger-Vink equation. From Table 6.2, it is clear that Mn-ions can act as a donor along with acceptor-type ions in the solid solution matrix. The favourable event can be concluded as the lowest D_r value; therefore, the most probable substitutions are Mn^{+2} ions at Nb^{+4}, Nb^{+5}, Cu^{+2} and Cu^{+1} sites and Mn^{+3} ions at Nb^{+4} and Nb^{+5} sites. In conclusion, acceptor-type substitutions are preferable to donor-type substitutions.

Table 6.2 Kröger-Vink notation defect equations for Mn-ion doping at Cu and Nb sites.

	Host site			
Dopant ion	Cu^{+1}	Cu^{+2}	Nb^{+4}	Nb^{+5}
Mn^{+2}	$Cu_{Cu} \rightarrow Mn_{Cu}^{\cdot} + e'$ **(D_r =12.9)**	$Cu_{Cu} \rightarrow Mn_{Cu}^{\times}$ **(D_r =8.2)**	$Nb_{Nb} \rightarrow Mn_{Nb}'' + 2h^{\cdot}$ **(D_r =1.4)**	$Nb_{Nb} \rightarrow Mn_{Nb}''' + 3h^{\cdot}$ **(D_r =4.6)**
Mn^{+3}	$Cu_{Cu} \rightarrow Mn_{Cu}^{\cdot\cdot} + 2e'$ (D_r =24.6)	$Cu_{Cu} \rightarrow Mn_{Cu}^{\cdot} + e'$ (D_r =20.5)	$Nb_{Nb} \rightarrow Mn_{Nb}' + h^{\cdot}$ **(D_r =14.7)**	$Nb_{Nb} \rightarrow Mn_{Nb}'' + 2h^{\cdot}$ **(D_r =9.3)**
Mn^{+4}	$Cu_{Cu} \rightarrow Mn_{Cu}^{\cdot\cdot\cdot} + 3e'$ (D_r =31.2)	$Cu_{Cu} \rightarrow Mn_{Cu}^{\cdot\cdot} + 2e'$ (D_r =27.3)	$Nb_{Nb} \rightarrow Mn_{Nb}^{\times}$ (D_r =22.0)	$Nb_{Nb} \rightarrow Mn_{Nb}' + h^{\cdot}$ (D_r =17.1)

The charged defect species can be of two types: (i) Point defects that can participate in conduction under the influence of the applied electric field (ii) Defect dipoles that can orient and align themselves in the presence of the electric field, contributing to the dipolar polarization. Defect dipoles can be formed between acceptor ion and oxygen vacancy ($Mn''_{Nb} - V_O^{\cdot\cdot}$) and between B site dipoles due to the substitution of ions such as $\left(Mn(+2)^{\cdot}_{Cu(+1)} - Mn(+3)'_{Nb(+4)}\right)$. The former is commonly known for inducing "hardness" in the material and is reported in many papers. The consequences of defect dipole formations are also reflected in the form of asymmetric increased coercive field, decreased conductivity and dielectric loss.

The common hypotheses behind the improvement of the physical properties of piezoelectric ceramics due to manganese doping are the following:

(i) They act as acceptor doping for the B-site cations having '+4' and higher valences due to the fluctuating Mn vacancies of '+2' and '+3' kinds. The acceptor type Mn-ion forms defect dipoles with oxygen vacancies, which tend to be created during high-temperature sintering in ceramics, containing volatile elements such as Bi and Pb. When an electric field is applied, these defect dipoles move and accumulate at grain boundaries and domain walls, and inhibit the switching of dipoles in opposite directions, thus inducing the so-called 'hardening effect' by pinning domain wall motion [151]. The formation of defect dipoles also reduces the overall conductivity of the materials by engaging the oxygen ion vacancies [146], but it also hinders the easy rotation of polarization.

(ii) Another possibility is that the doping of Mn acts as a donor ion for low valency cations present in the solid solution. By reducing the concentration of defect dipoles involving acceptor ions, donor doping induces mobilization of domains by de-pinning,

also called the ‘softening effect’. This doping can also improve densification and grain growth, which results in a domain size increment [145].

6.7 Temperature-Dependent Dielectric Studies on MnO_2 added (0.38)BCN-(0.62)PT Ceramics

Defects like “charged defect dipoles” and “point charge species” have a significant impact on the spontaneous polarization and conductivity of the dielectric materials. The overall internal field of dielectric material is contributed by both the unit cell polarization and the defect polarization. The resulting effects can be studied with the aid of temperature and frequency-dependent permittivity responses. Fig 6.7 shows the temperature dependence characteristics of the relative dielectric permittivity for (a) “Pure”, (b) Mn05, (c) Mn1, (d) Mn4 and (e) Mn8 ceramics measured at various frequencies. These graphs have multiple peaks that can be distinguished from one another according to how they vary with frequency.

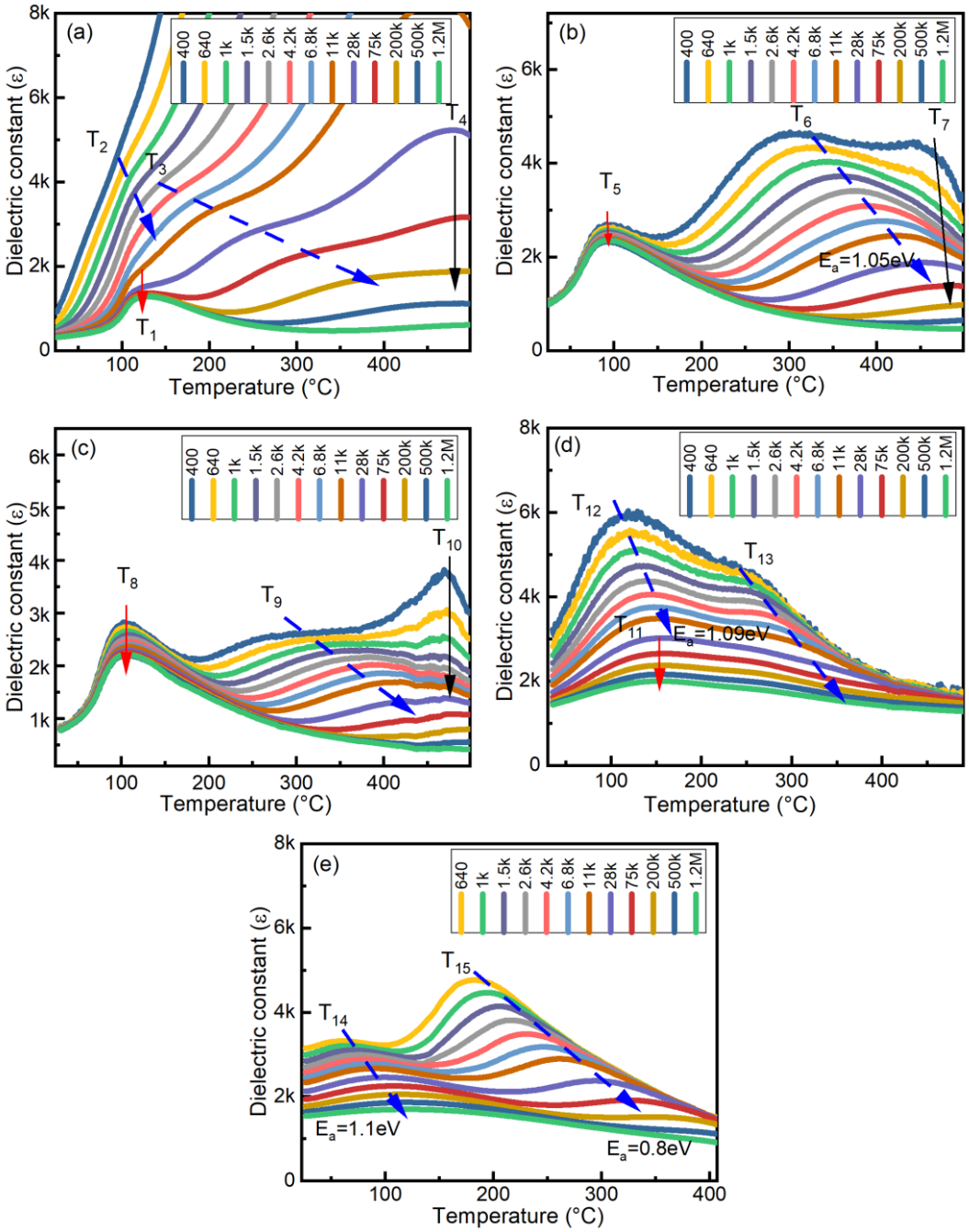

Fig 6.7 Temperature-dependent relative dielectric permittivity of (a) “Pure”, (b) Mn05, (c) Mn1, (d) Mn4 and (e) Mn8 compositions in the frequency range 0.4 kHz to 1.2 MHz

Two almost frequency-independent peaks are observed in Fig 6.7(a, b and c) corresponding to the “Pure”, Mn05 and Mn1 samples, respectively, around different temperature regions. First is around 90-150°C and another around 470-520°C. The first

one is marked by red arrows, viz., T_1, T_5 and T_8 correspond to the first transition and second one by black arrows for the second T_4, T_7 and T_{10}. The second peak is greatly masked by other defect-related relaxations, therefore its temperature-independent behaviour is somewhat unclear. Since there are non-centrosymmetric crystallographic phases in "Pure", Mn05 and Mn1 samples, the frequency-independent peaks can be attributed to their first order thermodynamic ferroelectric to paraelectric transitions. In Mn4, only one frequency-independent peak can be seen at the higher frequencies close to 150°C [see T_{11} in Fig 6.7(d)], corresponding to the ferroelectric to the paraelectric transition of the tetragonal phase of the material. The frequency-independent peaks are absent in the Mn8 sample [see Fig 6.7(e)] due to the cubic nature of its two coexisting phases. The additional relaxation peaks shown by the dotted blue arrows are mostly either the thermal activation of defect species to the external AC electric field or the responses of the NPRs of the polar clusters inside the cubic phases.

Higher dielectric constant values are observed at lower frequencies due to several contributions in permittivity such as interfacial space-charge polarisation, Maxwell-Wagner effect, intrinsic and extrinsic charged defects and so on [136,163]. At higher frequencies, the major contribution remains due to dipolar polarization. Therefore, a comparison of the dielectric permittivity of all the compositions at 1.2 MHz is shown in Fig 6.8(a). The Curie temperatures (T_c) of the "Pure", Mn05 and Mn1 are 128°C, 90°C and 107°C, respectively. Due to diffuse type transitions, the peak positions are not well defined in Mn4 and Mn8 compositions. Their diffusive character is driven by the NPRs, which are considerably masked by defect relaxation of the cubic phases. The temperature dependence of dielectric loss is shown in Fig 6.8(b). An enlarged image of the dielectric loss close to RT can be found in the inset of Fig 6.8(b).

The dielectric losses in Mn1 are low, which may be due to the asymmetric loop resulting from the formation of defect dipoles, leading to the breakage of the conduction path and increased resistivity of the material. The high losses in Mn4 and Mn8 compositions can be attributed to the high concentration of ions with variable valences that can increase the additional hole and electron carrier conductions, thus creating a local conduction path of long-range ordering within the material. This phenomenon lowers the overall resistivity and increases the dielectric losses. Out of all the compositions, the Mn1 shows a promising character with a high dielectric constant and the lowest dielectric loss. The P-E hysteresis loop measurements have been measured at RT and 50Hz frequency. The low frequency used in P-E measurement is not always sufficient to switch the defect dipoles along with it. However, if they acquire sufficient activation energy with the aid of high temperatures, the movement of defect species can be found in synchronisation with the applied field. Shifting of the permittivity peaks to higher temperatures with increased frequency is a manifestation of the dielectric relaxation process. Activation energy (E_a) values can be calculated by using the slope of the linearly fitted Arrhenius equation [equation (6.3)] for the logarithmic frequency of the corresponding peak temperature (T_p) in relative dielectric permittivity response.

$$\ln f = ln f_0 - \frac{E_a}{k_B T_p} \tag{6.3}$$

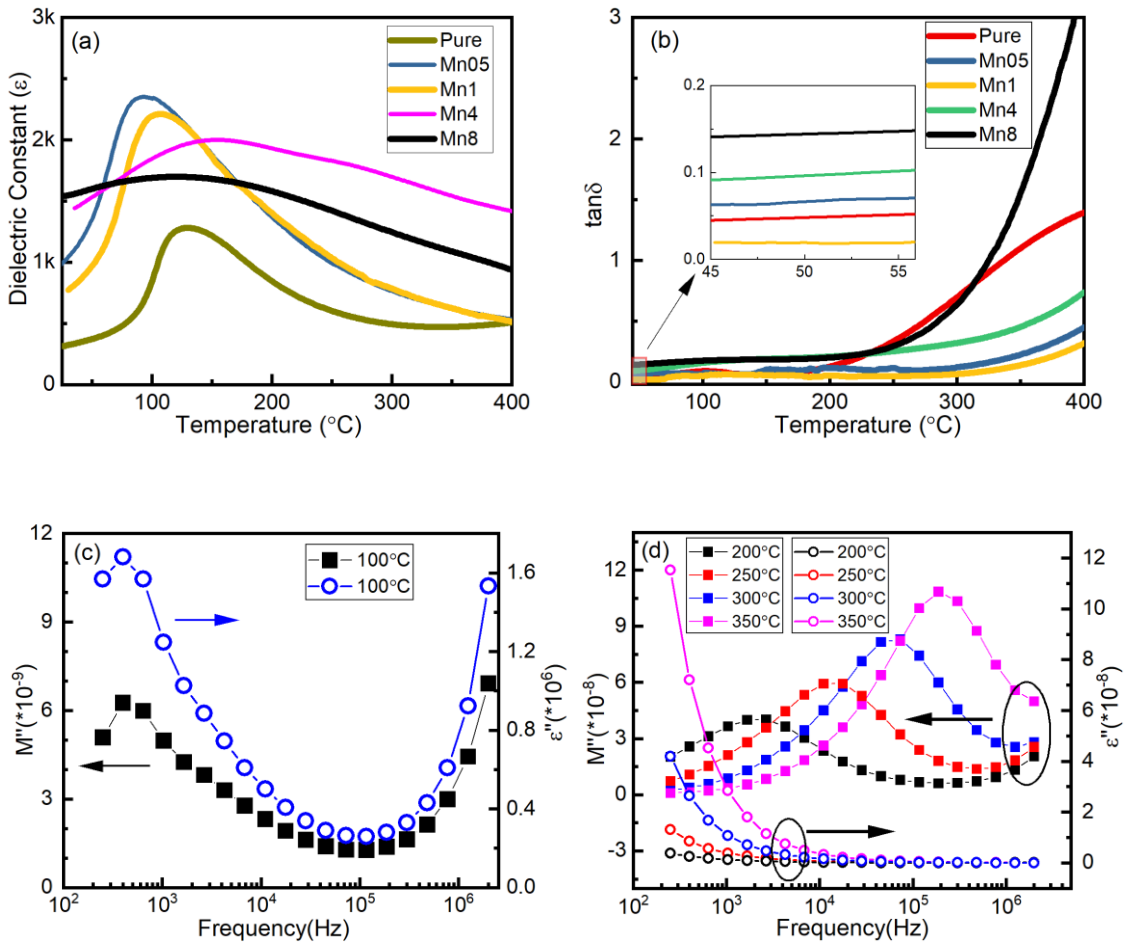

Fig 6.8 Temperature-dependent response of (a) dielectric constant and (b) loss for "Pure", Mn05, Mn1, Mn4 and Mn8 compositions at 1.2MHz, frequency-dependent response of the imaginary part of dielectric modulus ($M^{//}$) and the imaginary part of dielectric permittivity ($\varepsilon^{//}$) for Mn05 measured at (c)100°C and (d) 200°C, 250°C, 300°C and 350°C

In many similar perovskites, an activation energy of the order 1eV is reported for the relaxation related to oxygen vacancies [164]. The nearly comparable activation energies of 1.05eV in Mn05, 1.09eV in Mn4 and 1.1eV in Mn8 correspond to T_6, T_{12} and T_{14} relaxations (see Fig 6.7). Due to the overlapping of two kinds of peaks in Mn1, it is difficult to calculate their activation energies. The higher oxygen vacancy concentrations in XPS studies also lend weight to the aforementioned consideration. The other relaxation peaks in the temperature dependence of the dielectric response can

be associated with the conduction carriers (electrons and holes) due to ions with fluctuating valences in MnO_2-added samples.

To analyze the contribution of the dielectric share and conductivity share in the permittivity peak response, a simultaneous frequency-dependent study of the imaginary dielectric modulus ($M^{//}$) and the imaginary dielectric permittivity ($\varepsilon^{//}$) is conducted at various temperature regions. The dielectric modulus is a tool to characterise the relaxation processes in dielectric material. It help in separate the causes of dielectric relaxation, especially at high temperatures, which is hard to distinguish in complex impedance studies [165]. The expression of $M^{//}$ is given by the equation (6.4).

$$M'' = \frac{\varepsilon''}{[(\varepsilon')^2 + (\varepsilon'')^2]} \tag{6.4}$$

The apparent separation and minimal masking between the Curie transition and various peaks in the Mn05 sample led to its selection (see Fig 6.7). In Fig 6.8(c and d), its frequency-dependent $M^{//}$ and $\varepsilon^{//}$ responses have been plotted for different temperatures. The dielectric component is realized as having a peak in both the $M^{//}$ and $\varepsilon^{//}$ graphs for the same frequency range. Contrarily, the relaxations simulated by the conductive mechanisms only manifest as a peak in the $M^{//}$ graph and no such peak in the $\varepsilon^{//}$ graph with respect to the same frequency regions [166]. In Fig 6.8(c), both $M^{//}$ and $\varepsilon^{//}$ show peaks at similar frequencies; therefore, it is safe to say that the peak around 100°C in the permittivity response of Mn05 [Fig 6.7(b)] arises owing to the contribution of the dielectric part. Whereas, in Fig 6.8(d), the peaks are absent in $\varepsilon^{//}$ for the corresponding peak in $M^{//}$ for the higher temperature (>100°C) $\varepsilon^{//}$ responses. Hence, conductivity plays the main role in the permittivity peak appearance above 100°C in the form of relaxations in Mn05 composition.

6.8 Polarization Studies on MnO_2 added (0.38)BCN-(0.62)PT Ceramics

A ferroelectric bulk sample can only be used for polarization applications when operated below its breakdown strength. A lower leakage current passes through materials having good insulating characteristics with higher intrinsic breakdown strength. The DC breakdown strength of the (0.38)BCN-(0.62)PT of pure and MnO_2 additive samples are shown in Fig 6.9(a). The incorporation of the MnO_2 additive has certainly improved the breakdown strength, especially for low-concentration. A higher concentration of acceptor doping can further lead to enhanced conduction as for Mn4 [167]. Fig 6.9(b) shows the P-E hysteresis loops measured at RT at 50Hz on samples after poling. The typical loop of the pure (0.38)BCN-(0.62)PT sample is very lossy and does not show any ferroelectric nature due to its significantly large leakage current. An asymmetric P-E loop with a high coercive field has been observed for the samples with a low concentration of MnO_2 additive. This kind of favourable unipolar asymmetric polarisation could be caused by the poling process and presence of defect species [168]. An application of a strong DC field while poling encourages the defects to migrate and deposit at low energy regions such as grain boundaries and domain walls while aligning them parallel to the applied field. As a result, defects reduce the mobility of dipoles. Large pinning of domains is reflected in the form of asymmetric P-E loops for Mn05 and Mn1. In the higher concentrations of the MnO_2 additive, it is possible that favourable substitutions other than the acceptor type, such as Mn^{+2} at the Cu^{+1} site, have also occurred. The increased number of donor-type charged defects can thereby cause a reduction in the pinning of the domains. For Mn4 composition, a relatively high remnant polarization ($2P_r \sim 32\mu C/cm^2$) is noted, which can be attributed to increased charged species. Besides this, it also increases the dielectric loss and leakage currents in

the Mn4 sample. The P-E loop of Mn4 is slightly shifted to the right on the electric field axis. This shifting is attributed to the internal bias created by defect dipoles inside the material [142]. An internal bias field can be calculated by equation (6.2).

$$E_i = \frac{|E_{c+}| - |E_{c-}|}{2} \quad (6.2)$$

A biasing field of 2.68kV/cm is found in Mn4. A large decrement in the coercive field and remnant polarisation are observed in Mn8, resulting in a relaxor-type slim P-E loop. It suggests that the energy barrier between semiconducting grains and insulating grain boundaries is reducing. The de-pinning of domains results in the disappearance of the asymmetry in the respective hysteresis loop. The decreased polarization and increased breakdown strength in comparison to Mn4 suggest that Mn8 possesses fewer free charge carriers. An increase in the dielectric loss also supports this type of "softening effect" in Mn4 and Mn8. Fig 6.9(c) shows the MnO_2 concentration-dependent trends of P_r and E_c.

The relaxor character is induced by the high MnO_2 addition concentration in (0.38)BCN-(0.62)PT ceramic, which might be advantageous in energy storage applications. For instance, the Mn8 exhibits an energy storage density of 0.24 J/cm^{-3} with a high efficiency of ~68%. The efficiency can be anticipated to increase by further increasing Mn- content based on the trend of modifying P-E loops with MnO_2 concentration. In Fig 6.9(d), the transient switching current vs electric field loops corresponding to the P-E loops are shown. The overall polarization of a ferroelectric material determined by the P-E loop has contributions from the dipolar polarisation of bound charges, permittivity and current (free charges) [138]. The ferroelectric nature is attributed to the polarisation of bound charges in the form of dipoles and their reversal

with the switching field. The confirmation of polarisation contribution due to ferroelectric domain switching can be done by analysing the transient current graph along with the P-E hysteresis graph [138]. A characteristic peak in transient current appears corresponding to the domain flipping at a coercive field value, which suggests that the significant contribution in the P-E loop is due to ferroelectric domain switching. A monotonically increasing current profile suggests the contribution of conduction current by unbounded point-charged defects, whereas a flat kind of transient current response represents the influence of dielectric permittivity [138].

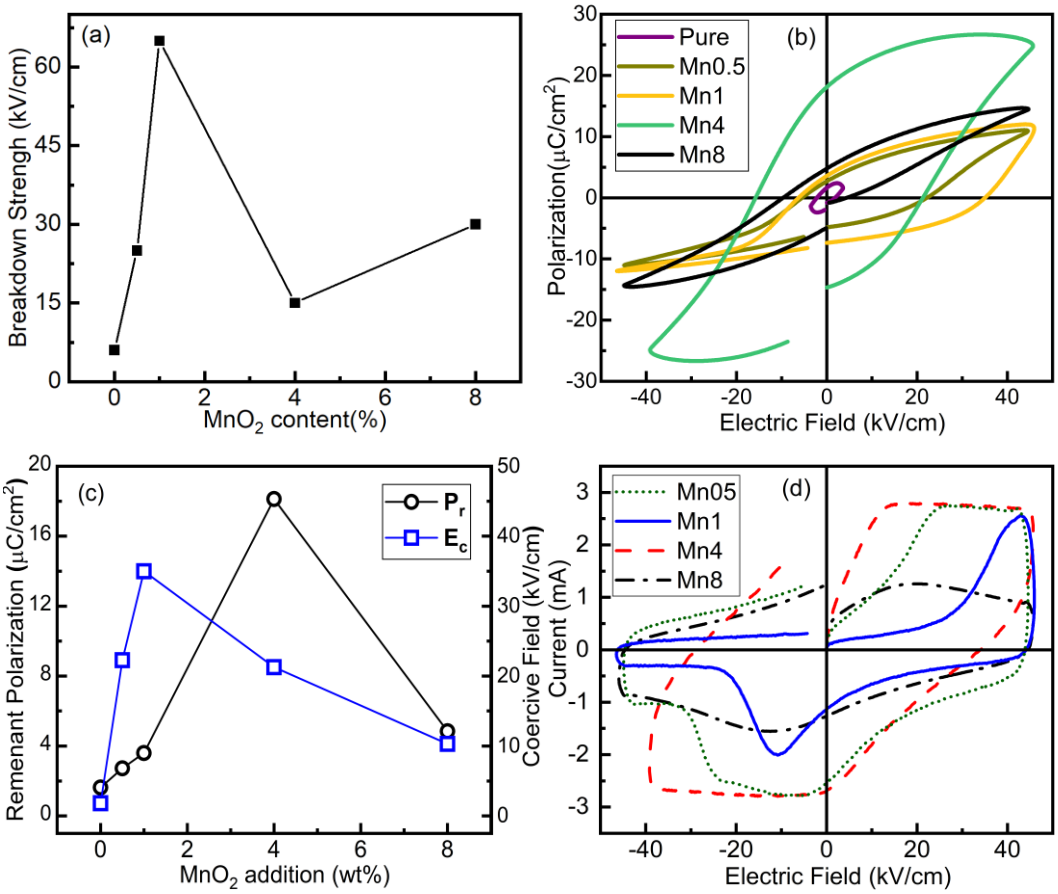

Fig 6.9 (a) Breakdown strength, (b) P-E hysteresis loops, (c) variation of remnant polarization and coercive field and (d) transient current vs electric field loops of MnO_2 added (0.38)BCN-(0.62)PT ceramics

In Mn1 and Mn8 compositions, the ferroelectric character is clearly observed due to the presence of the characteristic transient current peaks. Although the crystal structure of Mn8 composition is cubic, the existence of polarisation caused by NPRs with a relaxor ferroelectric nature can be expected in this material. The broadening of the transient current peak in Mn8 suggests the slight inclusion of a permittivity contribution. In Mn4 and Mn8, the paraelectric component can be seen as a straight line of y = mx type at low fields due to the conduction of the free-charged defects. For Mn05 and Mn4, the contribution of dielectric permittivity is high owing to the flat transient current profile compared to other compositions. The paraelectric or conduction contributions due to the charged defects are also high in Mn05 and Mn4. Although the remnant polarization has been greatly enhanced in Mn4, the respective current graph in Fig 6.9(d) demonstrates the contribution of dielectric permittivity along with domain switching more clearly. The Mn1 composition shows quite a promising ferroelectric character among all.

6.9 Piezoelectric Response of Pure and MnO_2 added (0.38)BCN-(0.62)PT Ceramics

Based on the XRD pattern of the poled sample, no modifications have been observed in the crystal structure in the samples after poling (not shown here). Thus, piezoelectricity caused by any electric field-induced crystallographic changes can be excluded. The piezoelectric response can be analyzed by weighing the crystal structural symmetry of as-prepared samples as well as the defect chemistry of the materials. Fig 6.10 displays the results of the measurement of direct piezoelectric strain coefficient (d_{33}) on the poled samples with varying MnO_2 contents at a frequency of 110Hz.

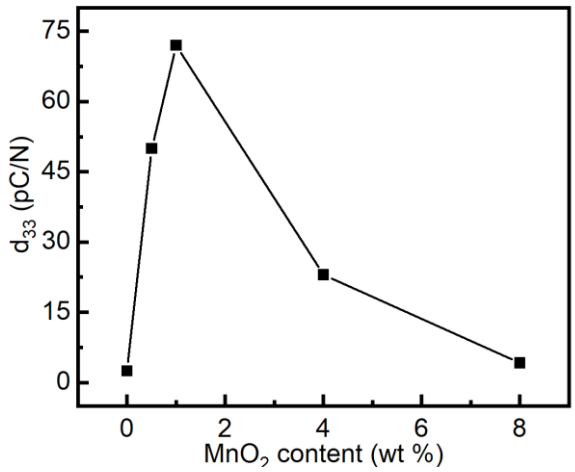

Fig 6.10 Variation of the direct piezoelectric strain coefficient (d_{33}) of pure and MnO_2 added (0.38)BCN-(0.62)PT ceramics

The piezoelectric response is greatly enhanced by only a small amount of MnO_2 addition. The highest d_{33} value of 72pC/N value has been obtained for Mn1 composition. The increased octahedral distortion, high breakdown strength and low dielectric loss collectively contribute to its behaviour. The d_{33} contribution of Mn4 may have come from the polarization from unit cell distortion [from phase 2(T)] as well as the NPR [co-existing relaxor phase 1(C)] since it possesses a coexisting crystal structure of tetragonal and cubic phases. The decreased breakdown strength, and lossy ferroelectric character, together with the reduced tetragonality and the reduced phase fraction of phase 2(T), contribute to the reduction of d_{33} in Mn4. Despite having a centrosymmetric crystal structure, Mn8 exhibits a minor amount of piezoelectricity (4pC/N), which may be attributed to the polarization contributions from NPRs. Additionally, a diffused relaxor-type transition in its relative dielectric permittivity response also supports the existence of NPRs.

6.10 Conclusion

The addition of MnO_2 is found to form defect-engineered compositions with significantly improved piezoelectric properties in (0.38)BCN-(0.62)PT system. The introduction of Mn-ions at the B-site in the perovskite lattice and the presence of its multiple ionization states have been confirmed by the XRD, EDS and XPS studies. The desirable properties have been tuned by optimizing the MnO_2 content in the solid solution. The (0.38)BCN-(0.62)PT composition possesses two co-existing phases whose tetragonal distortion and phase fractions can be effectively tuned by controlling the concentration of the MnO_2 additive. The 1wt% MnO_2 added (0.38)BCN-(0.62)PT ceramic has optimal piezoelectric, ferroelectric and dielectric properties with d_{33} = 72pC/N, ε_r = 836 (1kHz), tanδ = 0.03 (1kHz), P_r = 3.6μC/cm^2 and E_c = 35kV/cm. The high concentration MnO_2 addition is capable of inducing a relaxor nature in the pure ceramic, which can be used in energy storage applications. The energy storage density of 0.24J/cm^{-3} is observed in 8wt% MnO_2 added (0.38)BCN-(0.62)PT with ~68% efficiency. MnO_2 has been identified as a very effective additive for tailoring the crystal, structure, microstructure, dielectric, ferroelectric and piezoelectric properties of lossy dielectric materials.